Chemistry–A European Journal
Research Article
doi.org/10.1002/chem.202202361
Chemistry Europe
European Chemical Societies Publishing
www.chemeurj.org

Electrocatalytic CO_2 Reduction with a Binuclear Bis-Terpyridine Pyrazole-Bridged Cobalt Complex**

Antoine Bohn,[a] Juan José Moreno,[b] Pierre Thuéry,[c] Marc Robert,[a, d] and Orestes Rivada-Wheelaghan*[a, b]

In memory of Yehoshoa Ben-David.

Abstract: A pyrazole-based ligand substituted with terpyridine groups at the 3 and 5 positions has been synthesized to form the dinuclear cobalt complex **1**, that electrocatalytically reduces carbon dioxide (CO_2) to carbon monoxide (CO) in the presence of Brønsted acids in DMF. Chemical, electrochemical and UV-vis spectro-electrochemical studies under inert atmosphere indicate pairwise reduction processes of complex **1**. Infrared spectro-electrochemical studies under CO_2 and CO atmosphere are consistent with a reduced CO-containing dicobalt complex which results from the electroreduction of CO_2. In the presence of trifluoroethanol (TFE), electrocatalytic studies revealed single-site mechanism with up to 94% selectivity towards CO formation when 1.47 M TFE were present, at −1.35 V vs. Saturated Calomel Electrode in DMF (0.39 V overpotential). The low faradaic efficiencies obtained (<50%) are attributed to the generation of CO-containing species formed during the electrocatalytic process, which inhibit the reduction of CO_2.

Introduction

Mishandling of global resources has led to anthropogenic climate change.[1] To decrease its harmful effects and *Make Our Planet Great Again*,[2] shifts towards renewable energy storage,[3] circular feedstocks,[4] and energy-efficient processes are required.[5] Consequently, molecular electrocatalysis has experienced a renewed interest,[6–8] since it can contribute to sustainable and energy-efficient organic redox chemistry,[9–11] and to develop new strategies towards energy storage applications.[7,12] Along these lines, bimetallic electrocatalytic systems have been synthesized and studied aiming towards energy storage transformations,[13,14] such as water oxidation,[15] oxygen reduction,[16,17] hydrogen evolution reaction,[18–21] nitrogen reduction,[22] or carbon dioxide reduction[23] (Figure 1). Moreover, advances on the understanding of the structure and reactivity of metal-based cofactors has caused the growth of bioinspired multimetallic molecular systems,[13,24,25] to exploit their cooperative-reactivity potential.[26] A recent example of bioinspired bimetallic electrocatalysis for CO_2 transformation was recently published by Duboc et al., in which a NiFe-

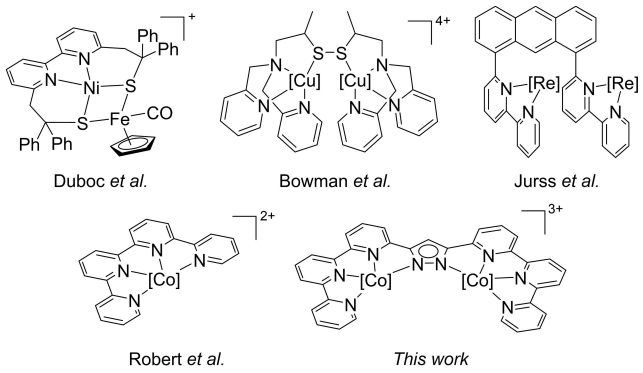

Figure 1. Bimetallic complexes used as electrocatalyst for the transformation of CO_2 (top). Monometallic cobalt electrocatalyst for CO_2 reduction and new dicobalt-based electrocatalyst for CO_2 reduction (bottom).

[a] *Dr. A. Bohn, Prof. M. Robert, Dr. O. Rivada-Wheelaghan*
Laboratoire d'Electrochimie Moléculaire
Université Paris Cité, CNRS
75006 Paris (France)
[b] *Dr. J. J. Moreno, Dr. O. Rivada-Wheelaghan*
Instituto de Investigaciones Químicas (IIQ)
Departamento de Química Inorgánica
Consejo Superior de Investigaciones Científicas (CSIC) and Universidad de Sevilla
Avenida Américo Vespucio 49, 41092 Sevilla (Spain)
E-mail: orivada@us.es
Homepage: https://oresteschem.wixsite.com/home
[c] *Dr. P. Thuéry*
NIMBE
Université Paris-Saclay, CEA, CNRS
91191 Gif-sur-Yvette (France)
[d] *Prof. M. Robert*
Institut Universitaire de France (IUF)
75005 Paris (France)

[**] *A previous version of this manuscript has been deposited on a preprint server (https://chemrxiv.org/engage/chemrxiv/article-details/61a8a288a02d16f623e114bc).*
Supporting information for this article is available on the WWW under https://doi.org/10.1002/chem.202202361
Part of a Special Collection to commemorate young and emerging scientists. To view the complete collection, visit Young Chemists 2022.

hydrogenase model promoted the conversion of CO_2 to CH_4 in aqueous solutions at pH 4 with 16% Faradaic efficiency (FE).[27] Another relevant example of bimetallic electrocatalyst was reported by Bowman et al., where a dicopper molecular system yielded 12 equivalents of oxalate from CO_2 at −0.03 V *versus* the normal hydrogen electrode.[28] As occurs with these two examples, metal-metal interaction has been rarely reported during molecular bimetallic electrocatalytic reduction of CO_2,[7,23] with cooperativity arising from bimetallic substrate activation in rare cases.[29] In this regard, pyrazole-based ligands are well-stablished platforms that allow such reactivity.[30] Under the right synthetic conditions, the deprotonated pyrazolate acts as an *exo*-bridge that generates the desired bimetallic complex. However, depending on the metal precursor and substituents at 3,5-positions at the N-heterocycle not only homo- or hetero-bimetallic complexes can be formed, but also mono- and polynuclear species.[30,31]

In our search for new molecular systems that can electrochemically activate and reduce CO_2,[32,33] we decided to synthesize a new bimetallic molecular complex bearing a pyrazole-core substituted with terpyridine groups at the 3,5-positions (Figure 1). Although this approach blocks the possibility of *exo*-bimetallic substrate activation,[34] ligands bearing a terpyridine fragment have shown the ability to reduce the overpotential for CO_2 electroreduction through metal-ligand cooperativity.[35–37] Additionally, the new synthesized ligand would generate a complex with structural similarities to species $[Co^{II}(qpy)(H_2O)_2]^{2+}$ (qpy = 2,2′:6′,2″:6″,2‴-quaterpyridine), which our group has thoroughly studied for the electrocatalytic CO_2 reduction reaction (Figure 1).[38–40] Thus, in this report we describe the synthesis and characterization of a new bimetallic molecular Co^{II}-complex. Additionally, we performed its electrochemical characterization under inert atmosphere and studied its electrocatalytic activity towards CO_2 reduction in the absence and presence of Brønsted acids, including its distinct behavior in different organic solvents.

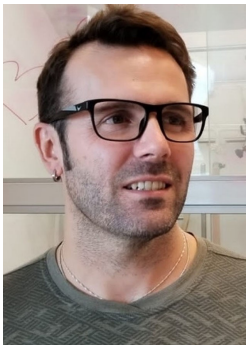

Orestes (1985-Seville) obtained his Ph. D. in inorganic chemistry at Universidad de Sevilla under the supervision of Dr. S. Conejero. He did postdoctoral stays with Prof. D. Milstein (Israel) at first and with Prof. J. Khusnutdinova (Japan) later, as JSPS Fellow. He was introduced to the theoretical and experimental techniques used in molecular electrochemistry as MOPGA Laureate at the Laboratoire d'Electrochimie Moleculaire, in collaboration with Prof. M. Robert (France). Since March 2022, Orestes works as a Ramón y Cajal Fellow at the Instituto the Investigaciones Químicas (Spain), targeting cooperative molecular electrocatalysts for chemical transformations with his team.

Results and Discussion

Ligand and complex synthesis and characterization

The pyrazole-based ligand, 3,5-bis{6-(2,2′:6′,2″-terpyridine)} pyrazole, **L-H**, has been characterized by NMR and high resolution mass spectrometry (HRMS) and was obtained in 30% yield, by reacting synthesized 6-methyl-2,2′:6′,2″-terpyridine carboxylate with 6-acetyl 2,2′:6′,2″-terpyridine, following reported procedures.[41] **L-H** exhibits low solubility in most solvents, presenting a symmetrical pattern in the ^1H and $^{13}C\{^1H\}$ NMR spectra, with the characteristic H-signal from the 4-position of the pyrazole ring appearing at 7.84 ppm in DMSO-d_6 (Figure S9). **L-H** was suspended in THF and deprotonated with 1.1 equivalents of ^{t}BuOK. Once a clear orange solution was formed, 2 equivalents of $CoCl_2$ were added, followed by 5 equivalents of $AgBF_4$ and MeCN, to facilitated the abstraction of the chloride atoms from the Co^{II}-coordination sphere. The reaction was stirred overnight protected from light inside the glovebox. Mixture purification generated the desired complex **1**, $[Co^{II}_2(L)(MeCN)_4][BF_4]_3$ in high yields, 90%. (Scheme 1).

Complex **1** crystallizes from concentrate MeCN/toluene solutions at room temperature, yielding large orange crystals suitable for single-crystal X-ray diffraction. As expected, the deprotonated ligand **L** binds to two Co^{II} atoms, where each center is six-coordinated and binds, besides the terpyridine fragment (terpy) and a N-atom from the pyrazolate, two N-atoms from coordinated MeCN at the apical positions. Thus, **1** is a tricationic dicobalt (II) complex, with **L** sharing a negative charge with both metal centers (Figure 2).

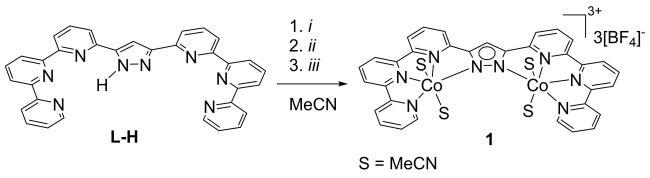

Scheme 1. Complex synthesis. *i*: 1.1 equivalent of ^{t}BuOK in THF; *ii*: 2 equivalents of $CoCl_2$ in THF; *iii*: 5 equivalents of $AgBF_4$ in MeCN.

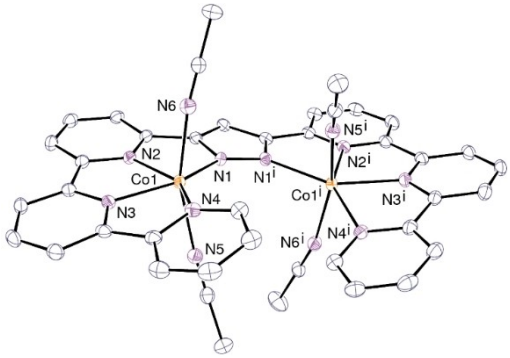

Figure 2. ORTEP view of complex **1**. Displacement ellipsoids are drawn at the 50% probability level and counterions, solvent molecules and hydrogen atoms are omitted. Symmetry code: i = 3/2−x, 3/2−y, z.

Complex **1** is paramagnetic and thus silent by ^{1}H NMR (μ_{eff} = 6.232 BM).[42] The effective magnetic moment observed is lower than the expected value for two S = 3/2 non-interacting spins at high-spin bimetallic octahedral Co^{II} complex,[43,44] might reflect the distorted octahedral geometry observed at each Co^{II}center.[45] Interestingly, previously reported bimetallic Co^{II} complexes stabilized with pyrazolate core ligands have shown antiferromagnetic coupling.[46] To gain insight into the electronic structure of **1**, we carried out DFT calculations at the B3LYP-D3(BJ)/6-311 + G(2d,p)//B3LYP-D3(BJ)/6-31 + G(d,p) level of theory in all accessible spin manifolds (from S = 0 to S = 3). We found that the high-spin configuration of the Co centers was preferred (S = 3). From this wavefunction, we then carried out broken-symmetry calculations to model antiferromagnetic coupling between the metal centers, which the regular closed-shell (S = 0) calculation could not address. We found that the broken simmetry singlet solution was isoenergetic with the S = 3 solution ($\triangle G_{qh}$ = 0.05 kcal/mol), suggesting that these two states are in equilibrium, which could explain the lower effective magnetic moment observed experimentally (Figure 3). We also found that the dissociation of bound acetonitrile molecules was thermoneutral (see Table S15).

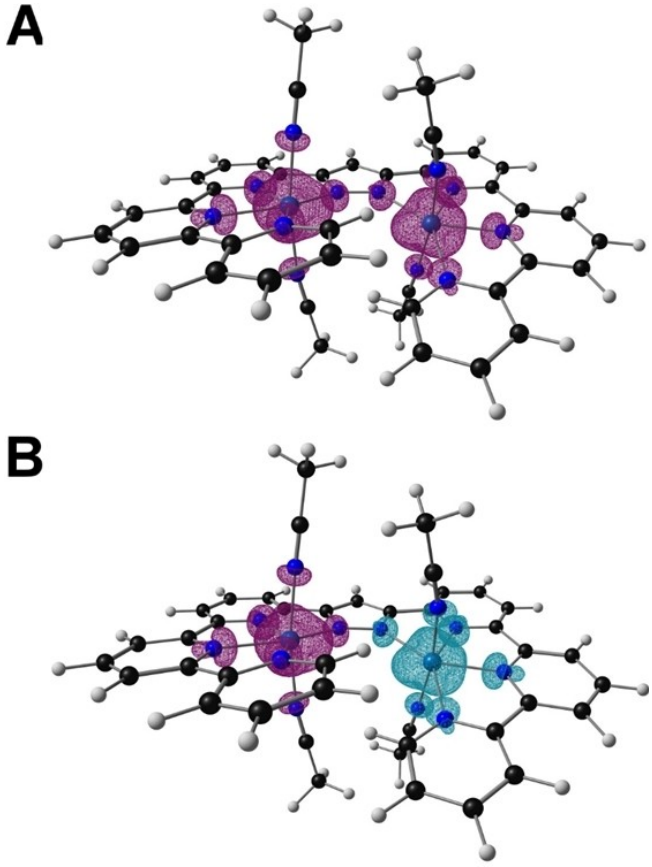

Figure 3. Spin densities of the isoenergetic septet (A) and antiferromagnetically coupled singlet (B) configurations.

Electrochemical studies under inert atmosphere

We analyzed the redox properties of complex **1** by cyclic voltammetry (CV). The electrochemical measurements were performed in dry solvents (MeCN or DMF) using a glassy carbon working electrode, a Pt-counter electrode, and a Saturated Calomel Electrode (SCE) as a reference electrode (at constant T = 293 K). Similarly to what is observed for the Co-quaterpyridine monometallic counterpart,[39] CV analysis of **1** (0.5 mM) in dry MeCN with 0.1 M Bu_4NPF_6 under Ar exhibited three difussion controled cathodic waves at −0.69 ($R1_{Ar}^{MeCN}$), −1.14 ($R2_{Ar}^{MeCN}$) and −1.56 ($R3_{Ar}^{MeCN}$) V vs. SCE (Figure 4). The value of the electron stoichiometry corresponding to the first electrochemical wave was determined by comparing the currents measured by chronoamperometry using microelectrodes and cyclic voltammetry using ultramicroelectrodes (Figures S21–S23).[47] Knowing the number of electrons involved at the first redox event in MeCN (2 electrons), we could determine the diffusion coefficient (D) of complex **1**. After variable scan rate analysis and application of the Randles-Sevcik equation, we obtained D = $2.1 \cdot 10^{-6}$ cm^2 s^{-1}.[48]

To gain further insight into the nature of the electrogenerated species, we performed thin-layer UV–vis spectroelectrochemistry (UV–SEC). As it can be observed in Figure 5, the spectra exhibit the appearance of 2 new broad absorption bands, centered at 400 and 500 nm (bordeaux), when the experiment was performed at a potential E = −0.85 V vs. SCE at room temperature under argon atmosphere. Being a reversible process, application of a potential E = 0.35 V vs. SCE forms back complex **1**, regenerating the initial spectrum (blue). Moreover, we analyzed by UV–vis the chemical reduction reaction of **1** with 2 equivalents of cobaltocene in MeCN since the one-electron redox potential of the cobaltocene/cobaltocenium couple falls between the $R2_{Ar}^{MeCN}$ and $R1_{Ar}^{MeCN}$ (E°_{CoCp2} = −0.9 V vs. SCE).[49] As it can be observed in Figure 5 (green trace), the spectrum is similar to that of the electrogenerated species

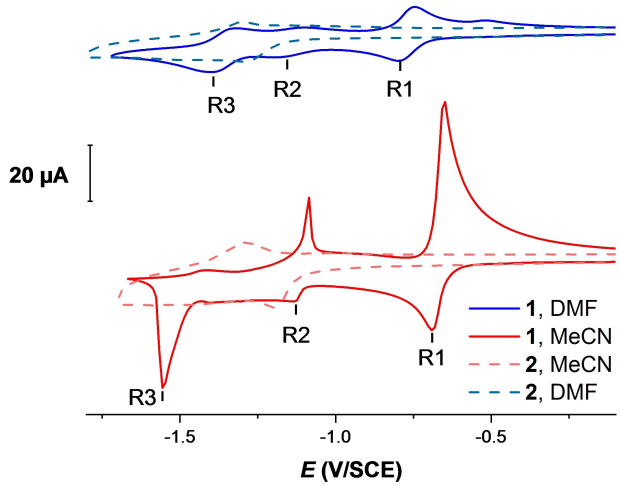

Figure 4. CVs of complexes **1** (line) and **2** (dotted line), 0.5 mM, in anhydrous DMF (blue) and MeCN (red) with 0.1 M of $TBAPF_6$, at 20 °C and scan rate of 0.1 V s^{-1}.

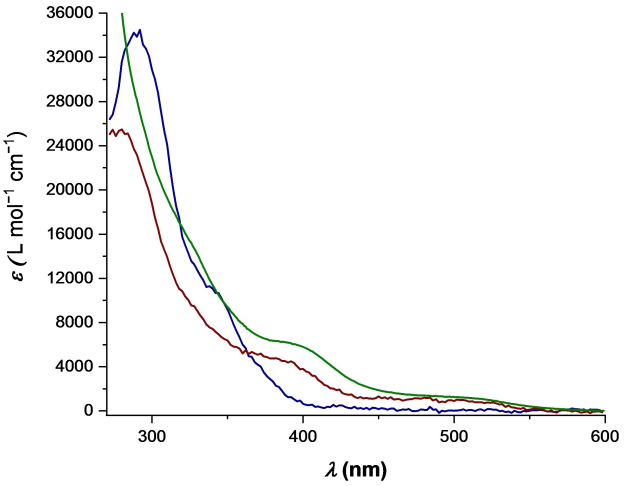

Figure 5. Blue: UV–vis spectrum of complex **1** in MeCN (0.1 M $TBAPF_6$). Bordeaux: UV–vis spectrum of electrogenerated species in MeCN (0.1 M $TBAPF_6$) at applied potential of −0.85 V vs SCE. Green: UV–vis spectrum from reacting complex **1** with 2 equivalents of cobaltocene in MeCN.

(bordeaux) in the visible region, supporting our assignment of a two-electron reduction process at $R1_{Ar}^{MeCN}$. Note that the high absorbance observed at 260 nm is due to the presence of 2 equivalents of cobaltocenium in solution.[50] Unfortunately, the reduced complex is unstable, leading to the disappearance of the bands when the solution is left for 30 min under Ar at room temperature. Consequently, attempts to isolate the reduced species through glovebox or Schlenk techniques proved unsuccessful.

We also investigated these reductions by computational means. For the one-electron reduced species the S = 5/2 state was found to be the lowest energy configuration. The highest SOMO is centered on one of the terpyridine fragments (Figure S63). Upon reduction, the cobalt center attached to the reduced terpyridine becomes low-spin, and is ferromagnetically coupled to the terpyridine-centered electron. Low-lying spin configurations encompassing an antiferromagnetically coupled terpyridine to high or low-spin cobalt centers were found to be slightly higher in energy (Table S16, Figures S64–65). As antiferromagnetic coupling between the metal centers was negligible in complex **1**, we did not explore electronic configurations where unpaired electrons on the two metal centers have opposite spins. These studies also suggest that solvent decoordination is facile (Table S16). In a similar fashion, the high-energy SOMO and SOMO-1 Kohn-Sham (KS) orbitals of the two-electron reduced complex are strongly centered on the terpyridine fragments, and the spin density plot is consistent with low-spin cobalt centers ferromagnetically coupled to terpyridine-centered radicals (Figure S66). As for compound **1**, configurations displaying antiferromagnetic coupling were close in energy to the S = 2 ground state (Figures S67–68, Table S17). Importantly, the calculated first two electron reductions occur with similar calculated standard redox potentials (−0.65 V vs. SCE, in excellent agreement with experiment), consistent with the assignment of a two-electron wave in CV.

Neither electrochemical methodologies nor thin-layer UV–SEC allowed us to determine the number of electrons involved at the second or third reduction waves, due to adsorption processes occurring at R2. Computational studies indicate that the third and fourth added electrons are also centered on the redox-active terpyridine fragments, with contributions from metal-based *d* orbitals (Figure S69). The triplet spin manifold (S = 1) was found to be the most stable configuration for the 4-electron reduced species (Table S19), comprising two low-spin Co(II) centers and two doubly reduced, singlet diradical terpyridine fragments. The S = 0 solution resulting from antiferromagnetic coupling between the Co centers was not investigated, as the high-spin complex **1** already presents negligible coupling.

CV analysis of **1** in dry DMF solution exhibits three diffusion controlled redox events at −0.79 ($R1_{Ar}^{DMF}$), −1.18 ($R2_{Ar}^{DMF}$) and −1.40 ($R3_{Ar}^{DMF}$) V vs. SCE (Figure 3, solid blue), without adsorption processes involved. To get insight in solvation effects, increasing amounts of DMF to a solution of **1** (0.5 mM) in MeCN were added (0.1 M $TBAPF_6$) and *vice versa*. While solutions of **1** in MeCN evolve gradually with the addition of DMF eventually generating a CV similar to those recorded in DMF (Figure S32), addition of MeCN to DMF solutions of **1** decreased the height of $R2_{Ar}^{DMF}$ with respect to $R3_{Ar}^{DMF}$ (Figure S31). The solvent-dependence electrochemical response of the bimetallic complex, as well as fast scan rate analysis in DMF (Figure S30), indicate a reductive electron stoichiometry of 2 ($R1_{Ar}^{DMF}$): 2 (combined $R2_{Ar}^{DMF}$ and $R3_{Ar}^{DMF}$) electrons for complex **1** (Figure S31–S32).[51] Furthermore, potentiostatic coulometry of complex **1** in DMF at −1.6 V vs. SCE yielded the consumption of four electrons (Figure S33). Finally, experimental evidence of ligand participation during the reduction process under inert atmosphere was obtained from CVs of complex **2** under similar conditions (Figure 4, dashed curves),[35,36] where complex **2** is the analogous to **1** and was synthesized and characterized reacting **L-H** with the non-redox active metal precursor [$Zn(OTf)_2$] (see Supporting Information).

Electrochemical studies under CO_2 atmosphere

Under CO_2 atmosphere in DMF, complex **1** exhibits catalytic current enhancement at potentials ca. −1.55 V, with a peak at ca. −1.90 V ($R4_{CO2}^{DMF}$, Figure 6, Top).[52] The slight shifting at the first cathodic wave ($R1_{CO2}^{DMF}$), as well as the current increase observed at the third cathodic wave ($R3_{CO2}^{DMF}$) is due to presence of traces of water, see below (Figures S56, S58 or S61). When $R4_{CO2}^{DMF}$ is reached, a new anodic wave at 0.28 V appears in the CV, which has been assigned to cobalt CO-containing species, since CVs performed under CO atmosphere presented the same anodic event (Figures S46–S48). Thus, indicating the requirement of 4-electron reduction to promote CO_2 reduction to CO. To obtain in situ information during the electroreduction of CO_2, infrared spectroelectrochemistry (IR-SEC) was performed from −1 to −2 V (vs. Ag wire) to solutions of complex **1** in DMF under CO_2 atmosphere. The spectra obtained from IR-SEC experiments at −1.6 V vs. Ag wire exhibited a new IR band at

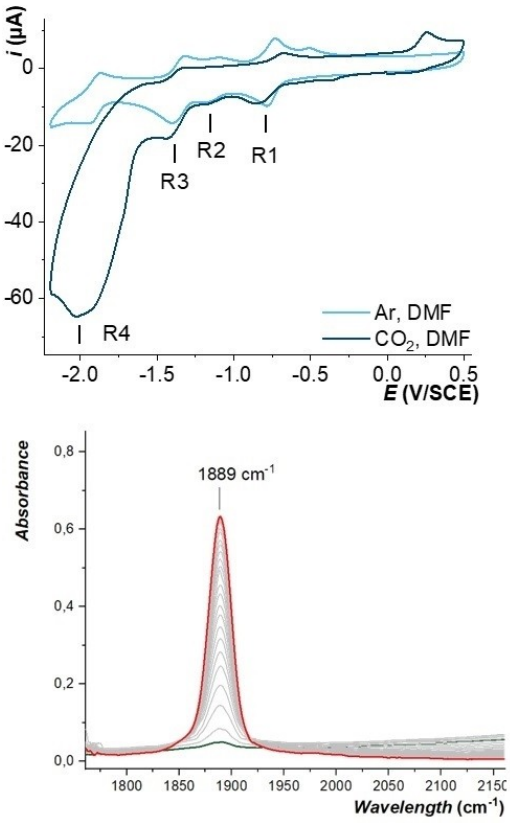

Figure 6. Top, CVs of complex **1** (0.5 mM) in anhydrous DMF with 0.1 M of $TBAPF_6$, at 20 °C and scan rate of 0.1 $V s^{-1}$, under argon (light blue) and CO_2 atmosphere (dark blue). **Bottom**, FT-IR-SEC spectra of a 0.5 M $TBAPF_6$/DMF solution of **1** (6 mM) under CO_2 at −1.6 V vs. Ag wire.

1889 cm^{-1}, assigned to a CO-containing dicobalt complex (Figure 6, Bottom). This band is not observed when complex **1** is dissolved in DMF and its IR measured under CO atmosphere. However, if a potential of −1 V vs. Ag wire is applied to this solution, the IR band at 1889 cm^{-1} is generated (Figure S50). Thus, we presume that the band corresponds to a reduced dicobalt carbonyl complex. This also agrees with the observed anodic wave at 0.28 V vs. SCE in DMF, see above (Figure 6, Top).

DFT calculations predict CO_2 binding to the 2-electron reduced species to be endergonic (+6.1 and +13.0 kcal/mol to bind one or two CO_2 molecules, respectively), with the binding of each CO_2 molecule is accompanied by the pairing of two electrons, one from the Co center and one from its terpyridine fragment, going from the S = 2 to manifold to S = 1 after one binding event (Figure S70) and to S = 0 after the second. In turn, in agreement with IR-SEC experiments, the binding of two CO molecules to the 2-electron reduced complex was found to be favorable by 4.2 kcal/mol (Figure S71). To gain further knowledge on the electrocatalytic activity, controlled potential electrolysis (CPE) of **1** (0.5 mM) in DMF was conducted at −2.05 V vs. SCE using a glassy carbon plate as the working electrode. The gaseous headspace of the sealed electrolysis cells was analyzed after the experiment, exhibiting non-substantial amounts of CO gas produced in DMF. During the first 15 minutes of CPE, the chronoamperogram exhibited rapid current inhibition. CV of the remaining DMF solution generated a similar current as prior to the CPE, indicating that the current decrease during CPE is due to electrode surface passivation (Table S3).

Electrochemical studies in the presence of Brønsted acids

Weak Brønsted acids have been shown to promote the catalytic electroreduction of CO_2,[53] by stabilizing the electrogenerated [M-CO_2] adduct and facilitating the cleavage of the C–O bond during the conversion to CO.[54] Since CO was detected during the electroreduction of CO_2 by **1**, we investigated the effects that different weak Brønsted acids such as water, phenol (PhOH) or TFE could impart.[52] Water addition during CV studies of **1** in DMF ($TBAPF_6$, 0.1 M) under CO_2 atmosphere shifted by 100 mV the cathodic wave $R1_{CO2}^{DMF,Water}$ to more negative potentials, indicating water coordination to the Co-centers (Figures 7A, S56 and S57).[39] Additionally, a new fivefold current increase in the electrocatalytic wave $R2_{CO2}^{DMF,\ Water}$ with respect to $R1_{CO2}^{DMF,\ Water}$ at ca. −1.35 V was observed.[55] During a 3 h CPE, under saturated CO_2 atmosphere at −1.4 V, 4 turnovers of CO and 5 of H_2 were generated (0.5 mM **1**, 0.5 M $TBAPF_6$ and 5 M water in DMF). However, heterogeneous catalysis arising from

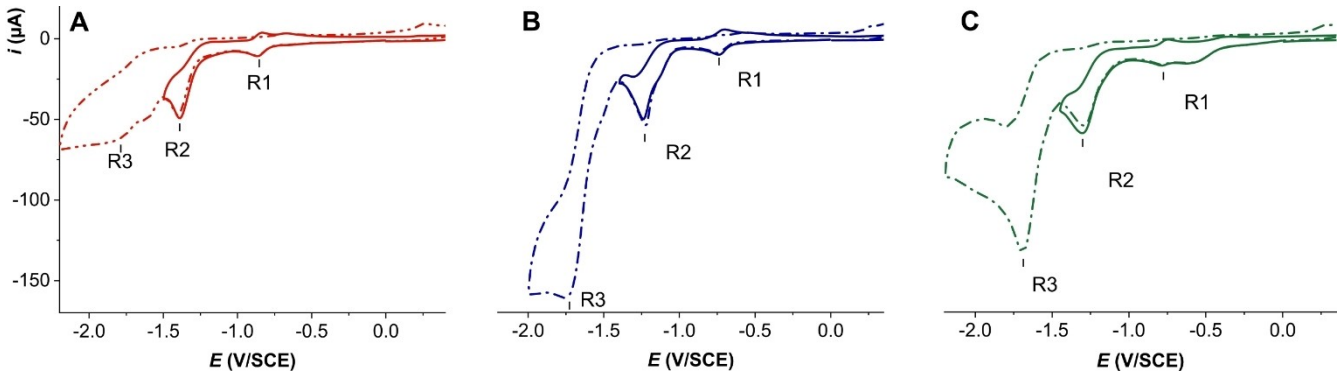

Figure 7. CVs of complex **1** (0.5 mM) under CO_2 atmosphere, in anhydrous DMF with 0.1 M of $TBAPF_6$, at 20 °C and can rate of 0.1 $V s^{-1}$, in the presence of 1.94 M of water (red), **A**; 3 M of PhOH (blue), **B**; and 1.47 M of TFE (green), **C**.

complex **1** derivatization/decomposition cannot be ruled out during CPE performance.[56] Indeed, CV analysis of the solution before and after CPE exhibited different redox behavior and rinse test analysis from the glassy carbon plate used during the CPE exhibited electrocatalytic activity (Table S4). Addition of PhOH to solutions of **1**, generated an electrocatalytic wave, $R2_{CO2}^{DMF,PhOH}$, at less negative potentials (ca. −1.23 V) with reversibility at $R1_{CO2}^{DMF,PhOH}$ (Figure 7B). CPEs performed at ca. −1.3 V in the presence of 3 M PhOH yielded higher CO TON (12) and less H_2 (TON = 3) than when water was present. Moreover, in the presence of PhOH a second large electrocatalytic wave ($R3_{CO2}^{DMF,PhOH}$) at ca. −1.75 V is observed in the CV (Figure 7B). A 3 h CPE under the same previous conditions but at −1.8 V applied potential generated more hydrogen (13 TON) keeping similar amounts of CO formed (12 TON).[57,58] As compared to water, the electrocatalytic response did improve at lower applied potentials, however heterogeneous pathways for electrocatalysis arising from electrocatalytically active material generated at the electrode surface during CPE cannot be ruled out (Table S5). Finally, addition of TFE to solutions of **1** generated a new prewave for $R1_{CO2}^{DMF,TFE}$ at ca. −0.55 V, with $R1_{CO2}^{DMF,TFE}$ exhibiting at slightly more positive potentials, plus an electrocatalytic wave $R2_{CO2}^{DMF,TFE}$ at ca. −1.3 V (Figure 7C). We were pleased to find that a 3 h CPE performed at −1.35 V (1.47 M TFE) yielded higher selectivity for CO conversion compared to water or PhOH (94%, 17 TONs of CO, 39% FE, and 1 TON of H_2). Using same conditions, CPE performed under $^{13}CO_2$ atmosphere generated ^{13}CO (Figure S62). From its rinse test analysis, CV before and after CPE and chronoamperogram's shape, we conclude that complex **1** presents higher stability under these last conditions. Likewise, after CPE performed for 1 h, the CVs remain almost identical (Table S11). Besides analyzing the gas space, after each CPE we analyzed the liquid phase by GC-MS, ionic chromatography, and NMR with different solvents (including DCl 37% in D_2O) without detecting other products arising from CO_2 reduction, solvent or supporting electrolyte degradation.

Although selectivity towards CO formation and TON were increased, while the overpotential remained rather low (390 mV),[38,59] the overall Faradaic efficiency did not exceed 50% in any case. These results contrast with what is observed for the more active monometallic Co-quaterpyridine complex, which produces same 17 TONs of CO (96% selectivity), however at lower potentials −1.1 V vs. SCE in MeCN solutions, with high FE (94%).[38] Studies under CO atmosphere indicate inhibition of the electrocatalytic activity of **1** (Figure S49). Thus, considering that inhibition could arise from strong CO binding to cobalt centers, we performed photoelectrocatalytic experiments under irradiation with 60 blue LED lamps (470 nm) to facilitate the CO release from the Co-center,[38,60] keeping the temperature of the cell controlled at 20 °C. These attempts did not improve the Faradaic efficiency of the catalysis (Table S12), neither experiments performed at higher temperature (Table S9).

Conclusion

We have described the synthesis of a new pyrazole-based ligand and formed and characterized a dinuclear cobalt (**1**) and zinc (**2**) complexes. From the experimental and computational studies presented, we propose a first 2 electron reduction process, followed by another second pairwise ligand-centered reduction for complex **1** under inert atmosphere. Our IR-SEC studies, electrocatalytic reduction of CO_2 in DMF the presence of TFE to generate CO, and DFT analysis suggests a mechanism for CO_2 electroreduction similar to those previously reported by Robert et al.,[38,39] and Head-Gordon et al.[36] involving the monometallic Co-quaterpyridine complex. Along these lines, the participation of the ligand framework containing terpyridine groups may facilitate the reduction of the overpotential.[35,36,38] Complex **1** exhibits higher stability when electrocatalysis is performed in DMF with 1.47 M of TFE, yielding 17 TONs of CO (94% selectivity) at −1.35 V vs. SCE in DMF (0.39 V overpotential).

Experimental Section

General specifications: All manipulations unless stated otherwise were performed using Schlenk or glovebox techniques under dry argon or nitrogen atmosphere, respectively. THF was dried over Na/benzophenone, freshly distilled prior to use and stored under nitrogen atmosphere over molecular sieves (4 Å). Anhydrous deuterated solvents were purchased from Eurisotop and stored over 4 Å molecular sieves. All chemicals unless noted otherwise were purchased from major commercial suppliers (TCI, Sigma-Aldrich, Across Organics) and used as received.

Cyclic voltammetry: The electrochemical experiments were performed under argon flow in a three-electrode cell. The working electrode was a steady glassy carbon electrode of approximately 0.07 cm^2 surface area, the counter electrode was a platinum wire, and the reference was a saturated calomel electrode separated from the solution by a bridge. The cyclic voltammograms (CVs) were recorded in dry *N*,*N*-dimethylformamide (DMF) and CH_3CN from Across Organics, using an AUTOLAB (Metrohm) PGSTAT100N potentiostat run with Nova 2.1.4 software. The electrolyte salt, tetrabutylammonium hexafluorophosphate ($TBAPF_6$) for electrochemical analysis, was purchased from Sigma-Aldrich and all the glassware was carefully dried before use.

Controlled Potential Electrolysis: Controlled potential electrolysis were conducted using a PARSTAT 4000A potentiostat (Princeton Applied Research). Preparative scale controlled potential electrolysis (CPE) experiments were performed in an electrolysis cell with a working compartment (4 mL liquid volume) and counter compartment (2 mL liquid volume) separated by an ultrafine glass frit, the total volume of the sealed cell is 39 mL, all CPEs were performed at +20 °C. A 2 cm^2 glassy carbon plate was used as the working electrode, a platinum grid was used as the auxiliary electrode, and a Saturated Calomel Electrode in a tipped glass tube filled with electrolyte ($TBAPF_6$, 0.5 M in DMF or CH_3CN) was used as a reference electrode. Both compartments were sealed to be gas-tight. A second glassy carbon electrode (0.03 cm^2 area) was added in the working compartment to perform CV scan before and after the CPE measurement. The working compartment was sparged with CO_2 for 10 min before adding the solutions. The electrolyte solution was constantly stirred during the CPE experiment with a 1 cm stirring bar. No iR compensation was applied. The electrolysis

experiments were then conducted at constant potential for the specified amount of time. After this period, the headspace of the cell was immediately analyzed by gas chromatography (GC).

Gas detection: GC analyses of gas sampled from the headspace during the electrolysis were performed with an Agilent Technologies 7820 A GC system equipped with a thermal conductivity detector. CO and H_2 production was quantitatively detected using a CP-CarboPlot P7 capillary column (27.46 m in length and 25 μm internal diameter). Temperature was held at 150 °C for the detector and 34 °C for the oven. The carrier gas was argon flowing at 9.5 mL/min at constant pressure of 0.4 bars. Injection was performed via a 250-μL gas-tight (Hamilton) syringe previously degassed with CO_2. Conditions allowed detection of both H_2, O_2, N_2, CO, and CO_2. Calibration curves for H_2 and CO were determined separately by injecting known quantities of pure gas. Detection limits for CO and H_2 are $5.2 \cdot 10^{-10}$ mol and $1.6 \cdot 10^{-10}$ mol, respectively.

UV-visible spectro-electrochemistry: This technique allows the in situ UV–vis characterization of intermediate species that are produced in the diffusion layer of an electrode. To do so, it is necessary to use a special cell, to which can be integrated three electrodes of the classical CV set-up, and that can be at the same time mounted in the spectrophotometer. The electrochemical cell is mounted in a special transparent Dewar-type support inside the spectrophotometer. The former consists of a 0.2 cm quartz UV–vis-NIR cell surmounted by a glass compartment. The Dewar was cooled, if needed, by a Julabo circulation cryostat. In this case, all experiments were conducted at 20 °C. We used the same set-up as previously described,[61,62] using a Toray carbon paper as working electrode with holes that allow light to pass through, connected with golden thread. This carbon material has a behavior much closer to the GC electrode than platinum, so the CV analysis can be directly correlated with the results in the spectroelectrochemical experiment. The reference electrode is a carbon/Teflon pseudoreference that is very stable for several hours, avoiding Ag^+ leaks in the solution that can be detrimental for electrochemistry experiments. Finally, a thin GC electrode has been integrated in the set-up, allowing the recording of CVs inside the cell. As a counter electrode, we use a platinum grid protected in a glass frit (Supporting Information, Figure S1). Absorbance spectra were collected using an Agilent Cary 60 UV–vis instrument.

Infrared spectro-electrochemistry: An optically transparent thin-layer electrode (OTTLE) cell, equipped with a CaF_2 window, Pt minigrid as working electrode, Pt microwire as counter electrode, and Ag microwire as a pseudo-reference electrode. For studies performed under CO_2 atmposphere, the blank solutions consist on the solution of **1** (6 mM) in DMF (0.5 M $TBAPF_6$) which later was used to substract the solvent signals. For experiments under CO atmosphere, the blank solutions was only electrolyte solution used to perform solvent subtractions. FT-IR spectra were measured using Perkin-Elmer FT-IR spectrometer.

NMR spectrometry: NMR spectra were measured on a Bruker Avance II 400 MHz spectrometer. The following abbreviations are used for describing NMR spectra: s (singlet), d (doublet), t (triplet), td (triplet of doublets), ddd (doublet of doublets of doublets), vd (virtual doublet), vt (virtual triplet), br (broad). Chemical shifts (δ_H, δ_C) were quoted in parts per million (ppm) and were referenced to the residual solvent peak.

Electrospray Ionization Mass Spectrometry (ESI-MS): The samples were solubilized in methanol or MeCN and then injected in direct introduction (infusion) in the mass spectrometer. A Bruker mass spectrometer, model micrOTOF-Q II was used with an electrospray source (ESI).

X-Ray crystallography: The data for **1** were collected at 100(2) K on a Bruker D8 Quest diffractometer equipped with an Incoatec Microfocus Source (IμS 3.0 Mo) and a PHOTON III area detector, and operated through the APEX3 software.[63] The data were processed with SAINT[64] and absorption effects were corrected for empirically with SADABS.[65,66] The structure was solved by intrinsic phasing with SHELXT[67] and refined by full-matrix least-squares on F^2 with SHELXL,[68] using the ShelXle interface.[69] All non-hydrogen atoms were refined with anisotropic displacement parameters. The hydrogen atoms were introduced at calculated positions and were treated as riding atoms with an isotropic displacement parameter equal to 1.2 times that of the parent atom (1.5 for CH_3). The molecular plot was drawn with ORTEP-3.[70]

Deposition Number 2106942 (for compound **1**) contain the supplementary crystallographic data for this paper. These data are provided free of charge by the joint Cambridge Crystallographic Data Centre and Fachinformationszentrum Karlsruhe Access Structures service.

Computational details: Geometry optimizationswere carried out with the Gaussian 09 Rev. E01 software package.[71] Optimizations were carried out without symmetry restrictions by using the B3LYP functional[72–75] that includes empirical dispersion corrections.[76] The 6-31+G(d,p) basis set[77–79] was used at the optimization stage; energies were corrected by means of single point calculations with the larger 6-311+G(2d,p) basis set. Bulk solvent effects (acetonitrile) were included during optimization with the SMD continuum model.[80] An ultrafine grid was used throughout the study.[81] Vibrational analysis was carried out on the stationary points to characterize them as minima or transition states the thermal corrections to enthalpy and free energy. Free energies were corrected (ΔG_{qh}) to account for errors associated with the harmonic oscillator approximation. Thus, according to Truhlars' quasi harmonic approximation, all vibrational frequencies below 100 cm^{-1} were set to this value so that the entropy contribution was not overestimated.[82] These anharmonic corrections were calculated with the Goodvibes code.[83] Kohn-Sham orbital projections and spin densities were plotted in ChemCraft with contour values of 0.03 and 0.005, respectively. Redox potentials were computed relative to the Fc^+/Fc pair and converted into SCE.[84]

Acknowledgements

The authors greatly acknowledge the financial support from the Investissement l'Avenir, specifically through the MOPGA call N° ANR-18-MPGA-0012 and the Spanish Ministerio de Ciencia e Innovación through the contract RYC-2020-028851 and Universidad de Sevilla through the talent attraction grant 2022/00000395.

Conflict of Interest

The authors declare no conflict of interest.

Data Availability Statement

The data that support the findings of this study are available in the supplementary material of this article.

Keywords: bimetallic · carbon dioxide · cobalt · electrocatalysis · spectro-electrochemistry

[1] The Intergovernmental Panel on Climate Change, **2021**.
[2] Make Our Planet Great Again, is an initiative of the President of the Republic of France Emmanuel Macron, Launched on 1st June 2017 following the decision of the United States to leave the Paris Agreement on the climate, **2017**.
[3] T. R. Cook, D. K. Dogutan, S. Y. Reece, Y. Surendranath, T. S. Teets, D. G. Nocera, *Chem. Rev.* **2010**, *110*, 6474–6502.
[4] J. H. Clark, T. J. Farmer, L. Herrero-Davila, J. Sherwood, *Green Chem.* **2016**, *18*, 3914–3934.
[5] A. Talaei, Md. Ahiduzzaman, A. Kumar, *Energy* **2018**, *153*, 231–247.
[6] J.-M. Savéant, *Chem. Rev.* **2008**, *108*, 2348–2378.
[7] N. W. Kinzel, C. Werlé, W. Leitner, *Angew. Chem. Int. Ed.* **2021**, *60*, 11628–11686; *Angew. Chem.* **2021**, *133*, 11732–11792.
[8] N. Wolff, O. Rivada-Wheelaghan, D. Tocqueville, *ChemElectroChem* **2021**, *8*, 4019–4027.
[9] P. De Luna, C. Hahn, D. Higgins, S. A. Jaffer, T. F. Jaramillo, E. H. Sargent, *Science* **2019**, *364*, eaav3506.
[10] Y. Kawamata, P. S. Baran, *Joule* **2020**, *4*, 701–704.
[11] C. Kingston, M. D. Palkowitz, Y. Takahira, J. C. Vantourout, B. K. Peters, Y. Kawamata, P. S. Baran, *Acc. Chem. Res.* **2020**, *53*, 72–83.
[12] K. E. Dalle, J. Warnan, J. J. Leung, B. Reuillard, I. S. Karmel, E. Reisner, *Chem. Rev.* **2019**, *119*, 2752–2875.
[13] Y. Zhao, G. Yu, F. Wang, P. Wei, J. Liu, *Chem. Eur. J.* **2019**, *25*, 3726–3739.
[14] Q. J. Bruch, G. P. Connor, N. D. McMillion, A. S. Goldman, F. Hasanayn, P. L. Holland, A. J. M. Miller, *ACS Catal.* **2020**, *10*, 10826–10846.
[15] X.-J. Su, M. Gao, L. Jiao, R.-Z. Liao, P. E. M. Siegbahn, J.-P. Cheng, M.-T. Zhang, *Angew. Chem. Int. Ed.* **2015**, *54*, 4909–4914; *Angew. Chem.* **2015**, *127*, 4991–4996.
[16] G. Passard, A. M. Ullman, C. N. Brodsky, D. G. Nocera, *J. Am. Chem. Soc.* **2016**, *138*, 2925–2928.
[17] S. Fukuzumi, S. Mandal, K. Mase, K. Ohkubo, H. Park, J. Benet-Buchholz, W. Nam, A. Llobet, *J. Am. Chem. Soc.* **2012**, *134*, 9906–9909.
[18] C. Di Giovanni, C. Gimbert-Suriñach, M. Nippe, J. Benet-Buchholz, J. R. Long, X. Sala, A. Llobet, *Chem. Eur. J.* **2016**, *22*, 361–369.
[19] K. K. Kpogo, S. Mazumder, D. Wang, H. B. Schlegel, A. T. Fiedler, C. N. Verani, *Chem. Eur. J.* **2017**, *23*, 9272–9279.
[20] M. G. Papanikolaou, A. Elliott, J. McAllister, J. K. Gallos, A. D. Keramidas, T. A. Kabanos, S. Sproules, H. N. Miras, *Dalton Trans.* **2020**, *49*, 15718–15730.
[21] S. Kal, A. S. Filatov, P. H. Dinolfo, *Inorg. Chem.* **2014**, *53*, 7137–7145.
[22] B. M. Lindley, R. S. van Alten, M. Finger, F. Schendzielorz, C. Würtele, A. J. M. Miller, I. Siewert, S. Schneider, *J. Am. Chem. Soc.* **2018**, *140*, 7922–7935.
[23] H. Chen, L. Chen, G. Chen, M. Robert, T. Lau, *ChemPhysChem* **2021**, *22*, 1835–1843.
[24] C.-H. Wang, S. DeBeer, *Chem. Soc. Rev.* **2021**, *50*, 8743–8761.
[25] A. L. Gavrilova, B. Bosnich, *Chem. Rev.* **2004**, *104*, 349–384.
[26] I. G. Powers, C. Uyeda, *ACS Catal.* **2017**, *7*, 936–958.
[27] M. E. Ahmed, S. Adam, D. Saha, J. Fize, V. Artero, A. Dey, C. Duboc, *ACS Energy Lett.* **2020**, *5*, 3837–3842.
[28] R. Angamuthu, P. Byers, M. Lutz, A. L. Spek, E. Bouwman, *Science* **2010**, *327*, 313–315.
[29] W. Yang, S. Sinha Roy, W. C. Pitts, R. L. Nelson, F. R. Fronczek, J. W. Jurss, *Inorg. Chem.* **2018**, *57*, 9564–9575.
[30] S. Trofimenko, in *Progress in Inorganic Chemistry*, John Wiley & Sons, Ltd, **1986**, pp. 115–210.
[31] J. Klingele, S. Dechert, F. Meyer, *Coord. Chem. Rev.* **2009**, *253*, 2698–2741.
[32] A. Srinivasan, J. Campos, N. Giraud, M. Robert, O. Rivada-Wheelaghan, *Dalton Trans.* **2020**, *49*, 16623–16626.
[33] E. Boutin, L. Merakeb, B. Ma, B. Boudy, M. Wang, J. Bonin, E. Anxolabéhère-Mallart, M. Robert, *Chem. Soc. Rev.* **2020**, *49*, 5772–5809.
[34] A. Brinkmeier, K. E. Dalle, L. D'Amore, R. A. Schulz, S. Dechert, S. Demeshko, M. Swart, F. Meyer, *J. Am. Chem. Soc.* **2021**, 10.1021/jacs.1c08645.
[35] J. S. Derrick, M. Loipersberger, R. Chatterjee, D. A. Iovan, P. T. Smith, K. Chakarawet, J. Yano, J. R. Long, M. Head-Gordon, C. J. Chang, *J. Am. Chem. Soc.* **2020**, *142*, 20489–20501.
[36] M. Loipersberger, D. G. A. Cabral, D. B. K. Chu, M. Head-Gordon, *J. Am. Chem. Soc.* **2021**, *143*, 744–763.
[37] S. Hooe, J. Moreno, D. Dickie, C. Machan, **2021**, 10.33774/chemrxiv-2021-lplvt.
[38] C. Cometto, L. Chen, P.-K. Lo, Z. Guo, K.-C. Lau, E. Anxolabéhère-Mallart, C. Fave, T.-C. Lau, M. Robert, *ACS Catal.* **2018**, *8*, 3411–3417.
[39] C. Cometto, L. Chen, E. Anxolabéhère-Mallart, C. Fave, T.-C. Lau, M. Robert, *Organometallics* **2019**, *38*, 1280–1285.
[40] L. Chen, G. Chen, C.-F. Leung, C. Cometto, M. Robert, T.-C. Lau, *Chem. Soc. Rev.* **2020**, *49*, 7271–7283.
[41] J. Pons, X. López, E. Benet, J. Casabó, F. Teixidor, F. J. Sánchez, *Polyhedron* **1990**, *9*, 2839–2845.
[42] D. H. Grant, *J. Chem. Educ.* **1995**, *72*, 39.
[43] S. I. G. Dias, A. I. S. Neves, S. Rabaça, I. C. Santos, M. Almeida, *Eur. J. Inorg. Chem.* **2008**, *2008*, 4728–4734.
[44] T. Ishida, T. Kawakami, S. Mitsubori, T. Nogami, K. Yamaguchi, H. Iwamura, *J. Chem. Soc. Dalton Trans.* **2002**, *16*, 3177–3186.
[45] S. Alvarez, *Chem. Rev.* **2015**, *115*, 13447–13483.
[46] S. Mandal, S. Shikano, Y. Yamada, Y.-M. Lee, W. Nam, A. Llobet, S. Fukuzumi, *J. Am. Chem. Soc.* **2013**, *135*, 15294–15297.
[47] C. Amatore, M. Azzabi, P. Calas, A. Jutand, C. Lefrou, Y. Rollin, *J. Electroanal. Chem. Interfacial Electrochem.* **1990**, *288*, 45–63.
[48] A. J. Bard, L. R. Faulkner, Electrochemical Methods: Fundamentals and Applications, 2nd Edition, Willey, **2001**.
[49] A. J. Bard, E. Garcia, S. Kukharenko, V. V. Strelets, *Inorg. Chem.* **1993**, *32*, 3528–3531.
[50] M. M. MacInnes, S. Hlynchuk, S. Acharya, N. Lehnert, S. Maldonado, *ACS Appl. Mater. Interfaces* **2018**, *10*, 2004–2015.
[51] D. A. Kurtz, D. Dhar, N. Elgrishi, B. Kandemir, S. F. McWilliams, W. C. Howland, C.-H. Chen, J. L. Dempsey, *J. Am. Chem. Soc.* **2021**, *143*, 3393–3406.
[52] Although, the electrochemical and electrocatalytic studies of complex **1** were performed in MeCN and DMF solutions. Due to non-diffusive effects and electrochemical adsoroption at the electrode surface when MeCN was used. The studies in MeCN solution have been located at the Supporting Information without further description.
[53] I. Bhugun, D. Lexa, J.-M. Savéant, *J. Am. Chem. Soc.* **1996**, *118*, 1769–1776.
[54] C. Costentin, S. Drouet, G. Passard, M. Robert, J.-M. Savéant, *J. Am. Chem. Soc.* **2013**, *135*, 9023–9031.
[55] J.-M. Savéant, C. Costentin, Elements of Molecular and Biomolecular Electrochemistry: An Electrochemical Approach to Electron Transfer Chemistry, Willey, **2019**.
[56] K. J. Lee, B. D. McCarthy, J. L. Dempsey, *Chem. Soc. Rev.* **2019**, *48*, 2927–2945.
[57] R. Francke, B. Schille, M. Roemelt, *Chem. Rev.* **2018**, *118*, 4631–4701.
[58] J. R. McKone, S. C. Marinescu, B. S. Brunschwig, J. R. Winkler, H. B. Gray, *Chem. Sci.* **2014**, *5*, 865–878.
[59] I. Azcarate, C. Costentin, M. Robert, J.-M. Savéant, *J. Am. Chem. Soc.* **2016**, *138*, 16639–16644.
[60] J. Lloret-Fillol, S. L. Fernández, S. Cañellas, F. Franco, J. M. Luis, M. À. Pericàs, *ChemElectroChem* **2021**, n.d., 10.1002/celc.202100859.
[61] N. Kostopoulos, F. Banse, C. Fave, E. Anxolabéhère-Mallart, *Chem. Commun.* **2021**, *57*, 1198–1201.
[62] N. Kostopoulos, C. Achaibou, J.-M. Noël, F. Kanoufi, M. Robert, C. Fave, E. Anxolabéhère-Mallart, *Inorg. Chem.* **2020**, *59*, 11577–11583.
[63] Bruker AXS, Bruker AXS. APEX3. Version 2019.1-0. Madison, Wisconsin, USA, 2019., **n.d**.
[64] Bruker Nano, Inc. SAINT. Version 8.40 A. Madison, Wisconsin, USA, 2019, **n.d**.
[65] Bruker AXS. SADABS. Version 2016/2. Madison, Wisconsin, USA, 2016, **n.d**.
[66] L. Krause, R. Herbst-Irmer, G. M. Sheldrick, D. Stalke, *J. Appl. Crystallogr.* **2015**, *48*, 3–10.
[67] G. M. Sheldrick, *Acta Crystallogr. Sect. A* **2015**, *71*, 3–8.
[68] G. M. Sheldrick, *Acta Crystallogr. Sect. C* **2015**, *71*, 3–8.
[69] C. B. Hübschle, G. M. Sheldrick, B. Dittrich, *J Appl Cryst* **2011**, *44*, 1281–1284.
[70] L. J. Farrugia, *J Appl Cryst* **2012**, *45*, 849–854.
[71] "G09 | Gaussian.com," can be found under https://gaussian.com/glossary/g09/, n.d.
[72] A. D. Becke, *J. Chem. Phys.* **1993**, *98*, 5648–5652.
[73] C. Lee, W. Yang, R. G. Parr, *Phys. Rev. B* **1988**, *37*, 785–789.
[74] S. H. Vosko, L. Wilk, M. Nusair, *Can. J. Phys.* **1980**, *58*, 1200–1211.
[75] P. J. Stephens, F. J. Devlin, C. F. Chabalowski, M. J. Frisch, *J. Phys. Chem.* **1994**, *98*, 11623–11627.

[76] S. Grimme, J. Antony, S. Ehrlich, H. Krieg, *J. Chem. Phys.* **2010**, *132*, 154104.
[77] W. J. Hehre, R. Ditchfield, J. A. Pople, *J. Chem. Phys.* **1972**, *56*, 2257–2261.
[78] P. C. Hariharan, J. A. Pople, *Theor. Chim. Acta* **1973**, *28*, 213–222.
[79] M. M. Francl, W. J. Pietro, W. J. Hehre, J. S. Binkley, M. S. Gordon, D. J. DeFrees, J. A. Pople, *J. Chem. Phys.* **1982**, *77*, 3654–3665.
[80] A. V. Marenich, C. J. Cramer, D. G. Truhlar, *J. Phys. Chem. B* **2009**, *113*, 6378–6396.
[81] A. N. Bootsma, S. Wheeler, **2019**, 10.26434/chemrxiv.8864204.v5.
[82] R. F. Ribeiro, A. V. Marenich, C. J. Cramer, D. G. Truhlar, *J. Phys. Chem. B* **2011**, *115*, 14556–14562.
[83] G. Luchini, J. Alegre-Requena, I. Funes, J. Rodríguez-Guerra, J. Chen, R. Paton, *Bobbypaton/GoodVibes: GoodVibes v3.0.0*, Zenodo, **2019**.
[84] V. V. Pavlishchuk, A. W. Addison, *Inorg. Chim. Acta* **2000**, *298*, 97–102.

Manuscript received: July 28, 2022
Accepted manuscript online: November 4, 2022
Version of record online: January 11, 2023